Physica B 695 (2024) 416542

Contents lists available at ScienceDirect

Physica B: Condensed Matter

journal homepage: www.elsevier.com/locate/physb

Unusual inverse spin Hall effect in Pt/Co/Pt multilayers on single-crystalline YIG

Feiyan Hou [a], Meiling Xu [a], Xuegang Chen [b], Yong Dong [b], Xiufeng Han [c], Tao Li [a,*], Xiangrong Wang [d,e,**], Tai Min [a,f,***]

[a] Center for Spintronics and Quantum Systems, State Key Laboratory for Mechanical Behavior of Materials, School of Materials Science and Engineering, Xi'an Jiaotong University, Xi'an, Shaanx, 710049, China
[b] Institutes of Physical Science and Information Technology, Anhui University, Hefei, Anhui, 230601, China
[c] Beijing National Laboratory for Condensed Matter Physics, Institute of Physics, University of Chinese Academy of Sciences, Chinese Academy of Sciences, Beijing, 100190, China
[d] Physics Department, The Hong Kong University of Science and Technology, Clear Water Bay, Kowloon, Hong Kong
[e] HKUST Shenzhen Research Institute, Shenzhen, 518057, China
[f] School of Materials Science and Intelligent Engineering, Nanjing University, Suzhou, 215163, China

ARTICLE INFO

Keywords:
Spintronics
Inverse spin Hall effect
Magnetic coupling
Magnetization reversal

ABSTRACT

The inverse spin Hall effect (ISHE) is a significant phenomenon that enables the conversion of spin current into charge current, offering promising applications in novel spintronic devices. In conventional ISHE measurements, it is widely recognized that the spin polarization, spin current, and generated charge current are mutually perpendicular. This study systematically investigates the ISHE in Pt/Co/Pt multilayers grown on a single-crystalline yttrium iron garnet (YIG) layer. A non-zero ISHE voltage was obtained along the direction parallel to the external magnetic field within the YIG coercive field range, deviating from the classical ISHE behavior. Our investigation revealed that the in-plane magnetic anisotropy of single-crystalline YIG plays a crucial role, as the easy axis of YIG and the external magnetic field collaboratively determine the polarization direction of the spin current, especially when the external magnetic field is smaller than the YIG coercive force. Furthermore, by tuning the small in-plane magnetization component of the Pt/Co/Pt multilayers, which couples with the YIG magnetization, we were able to control the shape and reversal path of the ISHE voltage loop. These findings deepen our understanding of how magnetic order affects charge current flow in ISHE measurements. The variety of ISHE voltage loop shapes and reversal paths observed suggest potential applications for this device as a magnetic field sensor.

1. Introduction

The spin Hall effect (SHE) is a fundamental spintronic phenomenon that converts a charge current into a spin current via spin-orbit interaction [1–3], playing a crucial role in energy-efficient data storage and energy harvesting applications [4]. Conversely, the inverse spin Hall effect (ISHE) converts a spin current into a charge current, enabling the electrical detection of spin currents [5–7]. Earlier studies in this field primarily focused on the heterostructures composed of ferromagnetic and nonmagnetic metal (NM) layers [8–12]. Where the ferromagnetic layer generates the spin current and the NM layer detects it. In recent years, ISHE [13] and SHE [14] have also been explored in ferromagnetic/antiferromagnetic heterojunctions. Yttrium iron garnet (YIG), a ferromagnetic insulator (FI) with low Gilbert damping and no contribution to the detected electrical signal, is widely favored as a spin current generator [15,16]. Spin current in YIG can be generated through microwave excitation or the spin Seebeck effect induced by a temperature gradient. Unlike ferromagnetic metal/NM heterostructures [17–20], where both spin and charge currents are present, YIG/NM bilayers inject a pure spin current into the NM layer without the

* Corresponding author.
** Corresponding author. Physics Department, The Hong Kong University of Science and Technology, Clear Water Bay, Kowloon, Hong Kong.
*** Corresponding author. Center for Spintronics and Quantum Systems, State Key Laboratory for Mechanical Behavior of Materials, School of Materials Science and Engineering, Xi'an Jiaotong University, Xi'an, Shaanx, 710049, China.
E-mail addresses: taoli66@xjtu.edu.cn (T. Li), phxwan@ust.hk (X. Wang), tai.min@mail.xjtu.edu.cn (T. Min).

https://doi.org/10.1016/j.physb.2024.416542
Received 22 July 2024; Received in revised form 10 September 2024; Accepted 11 September 2024
Available online 12 September 2024

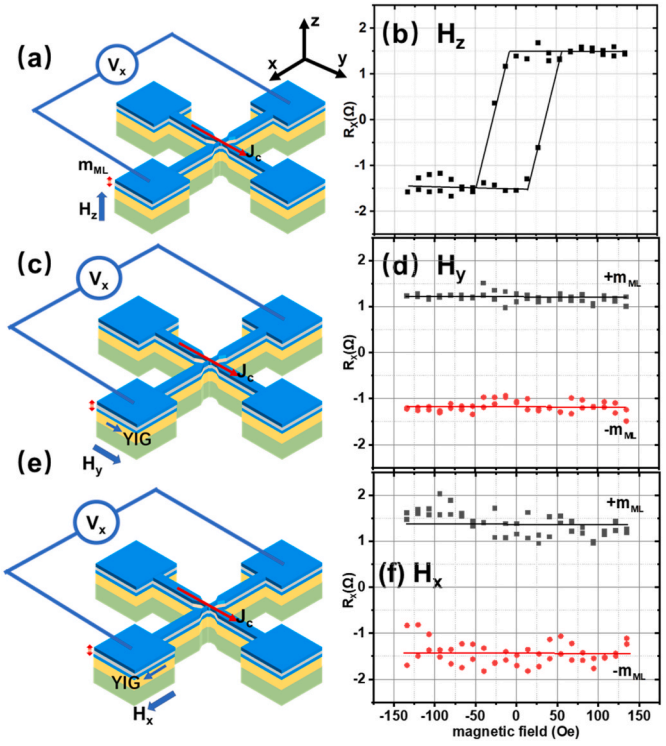

Fig. 1. The schematic illustrations depict the AHE measurement setups and corresponding results for the crossbar-patterned YIG/Pt/Co/Pt multilayer devices. The charge current is applied along the y-axis, the Hall voltage is measured along the x-axis, and the magnetic field is applied along the z-axis (a), y-axis (c), and x-axis (e), respectively. (b) The anomalous Hall resistance is measured with the magnetic field applied along the z-axis. The Hall resistance is measured while sweeping the magnetic field along the y-axis (d) and x-axis (f) with the $\boldsymbol{m}_{ML}$ aligned along either the positive (black) or negative z-axis (red). The solid lines along the data points serve as visual guides.(For interpretation of the references to colour in this figure legend, the reader is referred to the web version of this article.)

interference of an additional spin-polarized electron current, simplifying electrical measurements. Heavy metals with strong spin-orbit coupling (SOC) such as Pt, Ta, and W, are commonly employed for spin current detection [21]. In the conventional frameworks of SHE and ISHE, the spin polarization, spin current, and charge current are mutually orthogonal, imposing constraints on material systems for these applications.

By incorporating an additional magnetic layer with magnetization (M) oriented in specific directions into a classic FI/NM structure, the constraints of conventional ISHE can be overcome, leading to what is termed anomalous ISHE or magnetization-dependent ISHE [14,22–27]. Recently, Chuang et al. and Yagmur et al. reported magnetization-dependent ISHE in YIG/Pt/Co/Pt [24] and YIG/Pt/Tb_xCo_{100-x} [26], respectively, using thermally injected spin current via the spin Seebeck effect in YIG. Meanwhile, Yang et al. reported magnetization-dependent ISHE in YIG/Ti/$[Co/Pd]_5$ using spin pumping measurements [27]. In these studies, the mutual orthogonality of spin polarization, spin current, and charge current is disrupted due to the additional symmetry induced by the extra magnetic layers. Both polycrystalline [24,26]' and single-crystalline [27] YIG films were employed in these investigations. Furthermore, Huang et al. demonstrated that there is no difference in spin current generation efficiency between single-crystalline and polycrystalline YIG based on spin Seebeck experiments [28]. However, the presence of an easy axis in single-crystalline YIG results in distinct magnetization reversal behaviors under various orientations of an external magnetic field [29], potentially influencing the characteristics of the detected ISHE voltage loop.

In this study, we investigated the ISHE in the Pt/Co/Pt multilayers grown on a single-crystalline YIG layer. We observed a non-zero ISHE voltage (V_{ISHE}) parallel to the direction of the external magnetic field (H), attributed to the in-plane magnetic anisotropy of single-crystalline YIG, which is distinct from the magnetization-dependent ISHE reported in previous studies. Furthermore, our findings revealed that the in-plane magnetization component of the Pt/Co/Pt multilayer affects the reversal paths of the ISHE voltage loops along the direction of the external magnetic field. Despite the low coercive field ($H_c \approx 0.5$ Oe) of YIG, this device design enables clear differentiation of the magnetization reversal paths via the measured V_{ISHE} loop, highlighting its potential as an ultra-sensitive magnetic sensor.

2. Experiments and results

We fabricated YIG (80 nm)/Pt (2 nm)/Co (0.5 nm)/Pt (2 nm) heterostructures on gadolinium gallium garnet (GGG) substrates, which were subsequently fabricated into crossbar devices using photolithography and dry etching. The crystalline properties of YIG, characterized by X-ray diffraction (XRD), are shown in Fig. S4. The major diffraction peak at 51° indicates the single-crystal growth of the (111) plane. We verified the perpendicular magnetic anisotropy (PMA) of the Pt/Co/Pt multilayers on YIG by measuring the anomalous Hall resistance (R_x) following the method outlined in Ref. [30]. Since only the out-of-plane magnetization contributes to the anomalous Hall effect (AHE), this measurement allows us to track the magnetization direction of the Pt/Co/Pt multilayers ($\boldsymbol{m}_{ML}$) throughout the R_x measurements. The x- and y-axes were defined along the two directions of the crossbar, with the z-axis perpendicular to the sample surface. As shown in Fig. 1(a), a charge current of 0.3 μA was applied along the y-axis, and the Hall voltage was measured along the x-axis. By sweeping the out-of-plane magnetic field H_z, an AHE loop was obtained, as shown in Fig. 1(b). The coercivity of the Pt/Co/Pt multilayers is approximately 30 Oe, consistent with the vibrating sample magnetometer (VSM) results in Fig. S2(c). As shown in Fig. 1(d) and (f), R_x remains unchanged when sweeping magnetic field along either the y-axis (H_y) or the x-axis (H_x) within the range of ±140 Oe, as long as the $\boldsymbol{m}_{ML}$ is initialized along the positive or negative z-axis. Fig. S2(a) in the Supplementary Materials shows that the in-plane coercivity of YIG is approximately 0.5 Oe, much less than ±140 Oe. Therefore, we can switch the magnetization of YIG while keeping the $\boldsymbol{m}_{ML}$ unchanged. The inclined AHE loops in Fig. 1(b) indicate that the PMA of the Pt/Co/Pt multilayers is not perfectly aligned along the z-axis. Depending on the direction of the initializing magnetic field, the $\boldsymbol{m}_{ML}$ can be tilted toward the xy-plane. In this study, we used this tilted $\boldsymbol{m}_{ML}$ to control the magnetization reversal of YIG.

Next, we measured V_{ISHE} using the setup illustrated in Fig. 2 (a), where the sample was locally heated by laser irradiation on the Pt side, positioned at the center of the crossbar device. A continuous-wave laser with a wavelength of 800 nm was employed to heat the Pt surface, while the other side of the device remained at room temperature. The laser spot had a diameter of approximately 50 μm, and the laser power was maintained at 34 mW. Upon absorption of the laser energy, the device generated a thermal gradient ∇T of about 70 K/mm perpendicular to the sample plane, which, as reported, is confined laterally to the region surrounding the laser spot [31]. This thermal gradient induces a pure spin current J_s in the YIG film parallel to ∇T via the longitudinal spin Seebeck effect (SSE) [32], which is subsequently detected through the ISHE in the Pt/Co/Pt multilayers. The magnetic field was swept along the y-axis, and V_{ISHE} was measured along both the x- and y-axes.

The ISHE measurements were initially conducted on a crossbar device featuring a central ring-shaped structure. The optical image and dimensions of the device are presented in Supplementary Materials Fig. S3(a). The $\boldsymbol{m}_{ML}$ was initialized along the +z or -z-axis (Fig. 2(b)), and V_{ISHE} was first measured along the x-axis first. The procedure for initializing $\boldsymbol{m}_{ML}$ is illustrated in Fig. S1. Distinct V_{ISHE} loops were

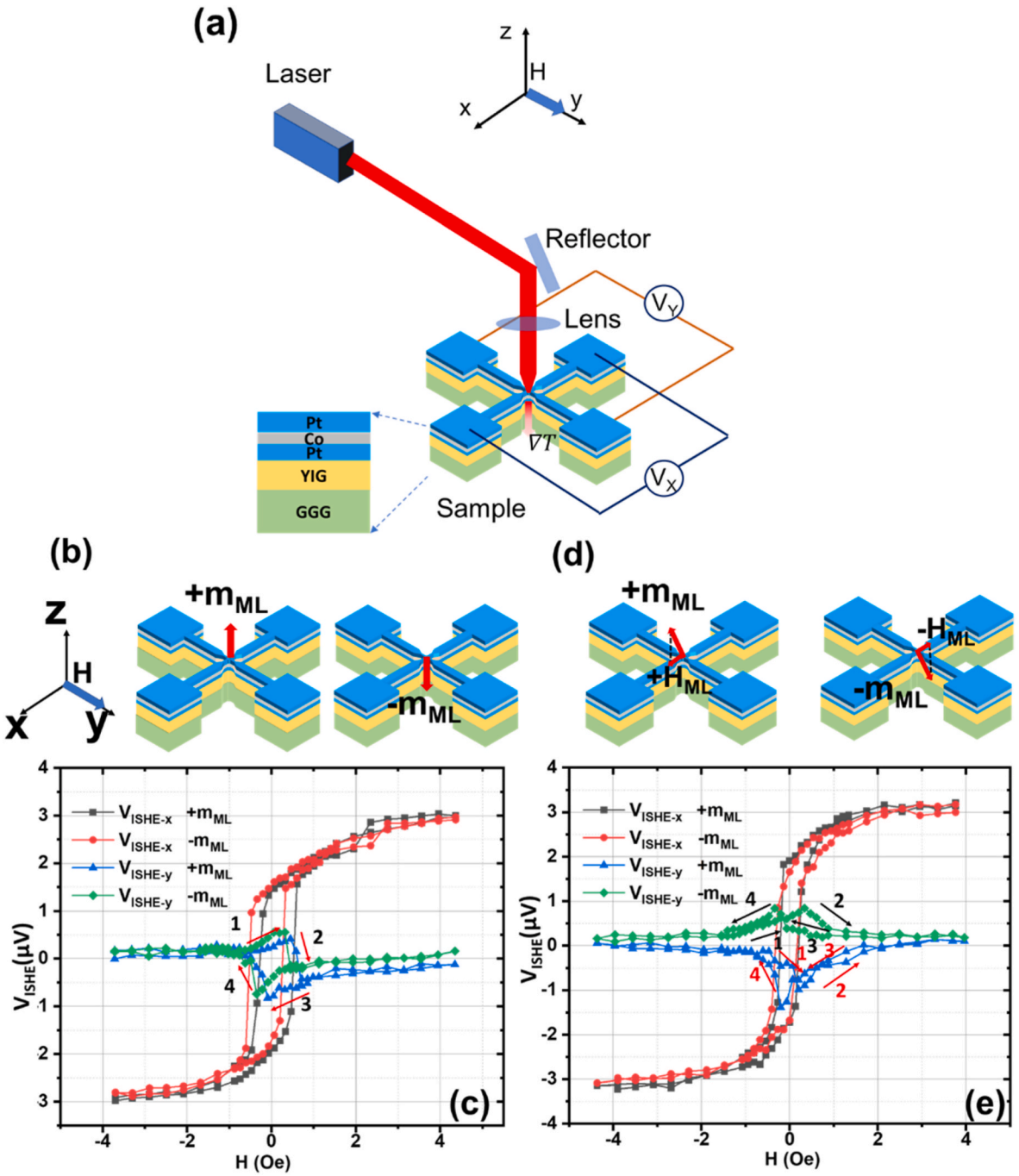

Fig. 2. The experimental setups for ISHE measurements and the corresponding results for the device with a central ring-shaped structure. (a) The schematic of the device and the V_{ISHE} measurement setups. A laser beam is focused at the center of the crossbar, creating a local thermal gradient ∇T perpendicular to the xy-plane. A sweeping magnetic field is applied along the y-axis, while V_{ISHE} along both the x- and y-axes are measured separately. (b) When $\boldsymbol{m}_{ML}$ is initialized along the positive or negative z-axis, and the measured V_{ISHE} along the x and y-axes is presented in (c). (d) When $\boldsymbol{m}_{ML}$ is initialized with a tilt, including a component along the positive or negative x-axis, the corresponding V_{ISHE} measurements are shown in (e).

observed, with a maximum $|V_{ISHE\text{-}x}| \approx 3$ μV at the saturation fields. Changing the direction of the initialized $\boldsymbol{m}_{ML}$ did not affect the shape of $V_{ISHE\text{-}x}$ loops, where the black-square and the red-dot curves correspond to $\boldsymbol{m}_{ML}$ initialized along the positive and negative z-axis, respectively (Fig. 2(c)). Unexpectedly, a non-zero $V_{ISHE\text{-}y}$ was observed along the y-axis when H was smaller than the coercive field of YIG (0.5 Oe). According to the relation $V_{ISHE} \propto \sigma \times J_S$, where σ is the spin-polarization unit vector and J_s is the spin-current induced by the thermal gradient, V_{ISHE} along the y-axis should theoretically be zero. The mechanism behind this unusual $V_{ISHE\text{-}y}$ behavior will be discussed in detail in the following section. Unlike the square-shaped hysteresis loop of $V_{ISHE\text{-}x}$, $V_{ISHE\text{-}y}$ loop exhibited an antisymmetric shape. Similar to $V_{ISHE\text{-}x}$, the reversal path of the $V_{ISHE\text{-}y}$ loop was independent of the magnetization direction of the initialized $\boldsymbol{m}_{ML}$, whether along the positive (blue triangles) or negative (green diamonds) z-axis.

In contrast, as illustrated in Fig. 2(d), tilting the $\boldsymbol{m}_{ML}$ towards the x-axis results in $+\boldsymbol{m}_{ML}$ having an effective magnetic field component ($+H_{ML}$) along the positive x-axis, while $-\boldsymbol{m}_{ML}$ has a component ($-H_{ML}$) along the negative x-axis. As shown in Fig. 2(e), a maximum $|V_{ISHE\text{-}x}| \approx 3$ μV was obtained at the saturation fields, and the shapes of $V_{ISHE\text{-}x}$ loops

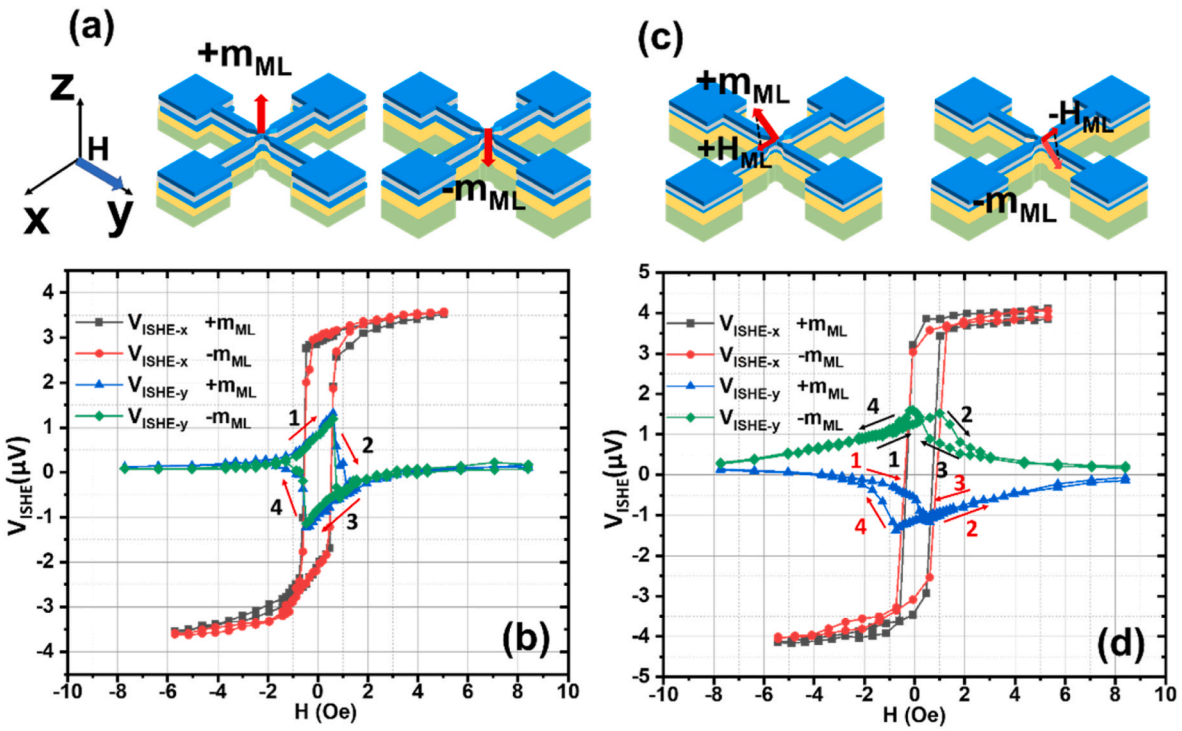

Fig. 3. ISHE experimental results from the device with a central cross-shaped structure. (a) The $\boldsymbol{m}_{ML}$ is Initialized along the positive or negative z-axis while the magnetic field H is swept along the y-axis. (b) The measured V_{ISHE} loops along the x-axis and y-axis. (c) The $\boldsymbol{m}_{ML}$ is initialized with a tilt, with a component along the positive or negative x-axis. The measured V_{ISHE} loops along the x- and y-axes are shown in (d).

remained unchanged regardless of the initialized $\boldsymbol{m}_{ML}$ direction, similar to the previous $V_{ISHE\text{-}x}$ measurements where $\boldsymbol{m}_{ML}$ had no x-axis component. However, the results of $V_{ISHE\text{-}y}$ significantly differed from the case without an additional $\boldsymbol{m}_{ML}$ component along the x-axis. $V_{ISHE\text{-}y}$ for $+\boldsymbol{m}_{ML}$ (blue triangles) and $-\boldsymbol{m}_{ML}$ (green diamonds) exhibited similar butterfly-shaped loops but in opposite directions. The turning points of these butterfly loops are located near the coercive field (H_c) of YIG.

The difference between the $V_{ISHE\text{-}y}$ loops in Fig. 2(c) and (e) can be attributed to the presence or absence of in-plane components in the $\boldsymbol{m}_{ML}$. When the $\boldsymbol{m}_{ML}$ aligns along the z-axis, $V_{ISHE\text{-}y}$ displays antisymmetric loops. However, when the $\boldsymbol{m}_{ML}$ tilts away from the z-axis, the $V_{ISHE\text{-}y}$ loops take on a butterfly shape. These results suggest a coupling between the in-plane component of $\boldsymbol{m}_{ML}$ and the magnetization of the YIG layer.

To verify whether the experimental results are influenced by the device geometry, we conducted the same experiments on a crossbar device without a central ring structure (Fig. S3(b)). The magnetization direction of the Pt/Co/Pt multilayers and the corresponding experimental results are shown in Fig. 3. The key characteristics observed in this device are consistent with those from the previous device, as presented in Fig. 2. Therefore, the $\boldsymbol{m}_{ML}$-manipulated $V_{ISHE\text{-}y}$ hysteresis loop shapes are independent of the device geometry.

3. Discussion

In addition to ISHE, other thermal voltages may contribute to the measured V_{ISHE}. To clarify their effects, we conducted a systematic analysis. First, radially symmetric thermal gradients within the sample plane result in the cancellation of their contributions to the thermoelectric effect, such as the Seebeck effect [33]. However, if the light spot is off-center on the crossbar, an asymmetric heat distribution may create an in-plane thermal gradient. To prevent this, we used a charge-coupled device (CCD) to observe the laser spot's position before measuring V_{ISHE}. We then adjusted the three-dimensional (3D) translation stage, ensuring the laser spot was centered on the crossbar device. The second step involved fine-tuning the stage so that the absolute values of $V_{ISHE\text{-}x}$ were equal at both positive and negative saturation magnetic fields. These experimental procedures minimize the thermal voltage caused by in-plane thermal gradient.

Secondly, when the $\boldsymbol{m}_{ML}$ has an in-plane component, the thermal gradient along the z-axis may induce an anomalous Nernst voltage (V_{ANE}) along the y-axis, which can superimpose on the measured $V_{ISHE\text{-}y}$ [34]. However, due to the limited temperature gradient within the Pt/Co/Pt layer and the small in-plane magnetization component, this voltage is minimal. Another important factor is that V_{ANE} changes with the reversal of Pt/Co/Pt magnetization. In our experiment, the maximum scanned magnetic field range was ±8 Oe, which is insufficient to reverse the magnetization of Pt/Co/Pt. Therefore, the V_{ANE} superimposed on $V_{ISHE\text{-}y}$ remains constant and does not affect our analysis of the behavior of $V_{ISHE\text{-}y}$ loop under the changing magnetic field. To confirm that the measured voltage primarily originates from ISHE, we analyzed the variation of $V_{ISHE\text{-}x}$ with laser power and its behavior at different angles between the magnetic field and the x-axis, as shown in Figures S5~7. Additionally, while the ANE can be induced by the magnetic proximity effect in Pt, previous studies have shown that in Pt/YIG systems, the thermal voltage is primarily due to the spin current from the longitudinal spin Seebeck effect (SSE), with negligible contribution from proximity-induced ANE [35,36].

Thirdly, Ellsworth et al. suggested that photons exerted on Pt in close proximity to YIG can generate a spin voltage, known as the photo-spin-voltaic (PSV) effect [37]. It was shown that light with a wavelength in the range of 700 nm $< \lambda <$ 1000 nm makes a negligible contribution to the PSV effect. Since the wavelength we used (800 nm) falls within this range, the PSV effect is expected to be negligible in our experiments. Last but not least, while Pt/Co magnetic heterostructures can generate spin and charge currents under ultrafast femtosecond pulse lasers excitation [38–41]. However, we used a continuous wave laser instead of a pulsed laser in our experiment so that laser-excited spin and charging currents should not occur.

To gain further insight into the observed phenomena, we applied the classical Stoner-Wohlfarth model to analyze our experimental results.

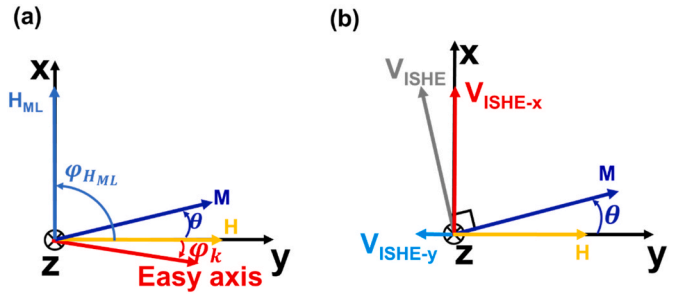

Fig. 4. The schematic diagram of the Stoner-Wohlfarth model. (a) The relative directions of the external sweeping magnetic field (H), the magnetization vector of YIG (M), and the in-plane component of $\boldsymbol{m}_{\mathrm{ML}}$ (H_{ML}). (b) The V_{ISHE} generated by ISHE and its components of $V_{ISHE\text{-}x}$ and $V_{ISHE\text{-}y}$.

The in-plane angle-dependent YIG hysteresis loops, measured using VSM are shown in Fig. S2(b), revealing that the YIG film exhibits in-plane magnetic anisotropy. During the ISHE measurements, the effective magnetization direction of YIG is influenced by its in-plane magnetic anisotropy, the external sweeping magnetic field H, and the in-plane component of $\boldsymbol{m}_{\mathrm{ML}}$. As illustrated in Fig. 4(a), within the xy-plane, H denotes the sweeping magnetic field, M represents the magnetization of the YIG, and the in-plane component of the magnetization of Pt/Co/Pt multilayers acts as an effective magnetic field H_{ML}. The orientation of YIG magnetization M is determined by the minimum magnetic energy density [42]:

$$E = E_A + E_Z = K\sin^2(\varphi_k - \theta) - HM\cos(\theta) - H_{ML}M\cos(\theta - \varphi_{H_{ML}}) \quad (1)$$

where E_A is the anisotropy energy and E_Z is the Zeeman energy. As shown in Fig. 4(a), H is aligned along the y-axis and φ_{HML} represents the angle between H_{ML} and the y-axis. We set H_{ML} to be aligned along the x-axis, making $\varphi_{HML} = 90°$. θ is the angle between M and the y-axis, and φ_k is the angle between the easy axis and the y-axis. Since H_{ML} and φ_k cannot be directly measured, we used various values in the simulation. When $H_{ML} = 0.2$ Oe and $\varphi_k = 5°$, the calculated result was closest to the experimental data. Fig. S8 shows the theoretical V_{ISHE} for different values of H_{ML}. $K = \frac{M_s H_k}{2}$ denotes the anisotropy constant of YIG, where M_s is the saturation magnetization and H_k is the anisotropy field. Based on the VSM measurements, we used $M_s = 83$ emu/cm^3. The angle between H and the easy axis is 5°, so $H_k \approx H_c = 0.5$ Oe.

According to the relation $V_{ISHE} \propto \sigma \times J_S$, V_{ISHE} is perpendicular to M as shown in Fig. 4(b). In the experiment, we measured V_{ISHE} along both the x- and y-axes, which can be expressed as:

$$V_{ISHE-x} = V_{ISHE}\cos(\theta) \quad (2)$$

$$V_{ISHE-y} = V_{ISHE}\sin(\theta) \quad (3)$$

When $H_{ML} = 0$, Fig. 5(a) and (b) illustrate how θ changes with the sweeping of H. The results indicate that θ follows the same path regardless of whether $\boldsymbol{m}_{\mathrm{ML}}$ is aligned along the positive or negative z-axis, suggesting that the reversal of YIG magnetization occurs along the same trajectory. The normalized $V_{ISHE\text{-}x}$ and $V_{ISHE\text{-}y}$ are shown in Fig. 5 (c) and (d), where the $V_{ISHE\text{-}y}$ loops exhibit antisymmetric shapes that

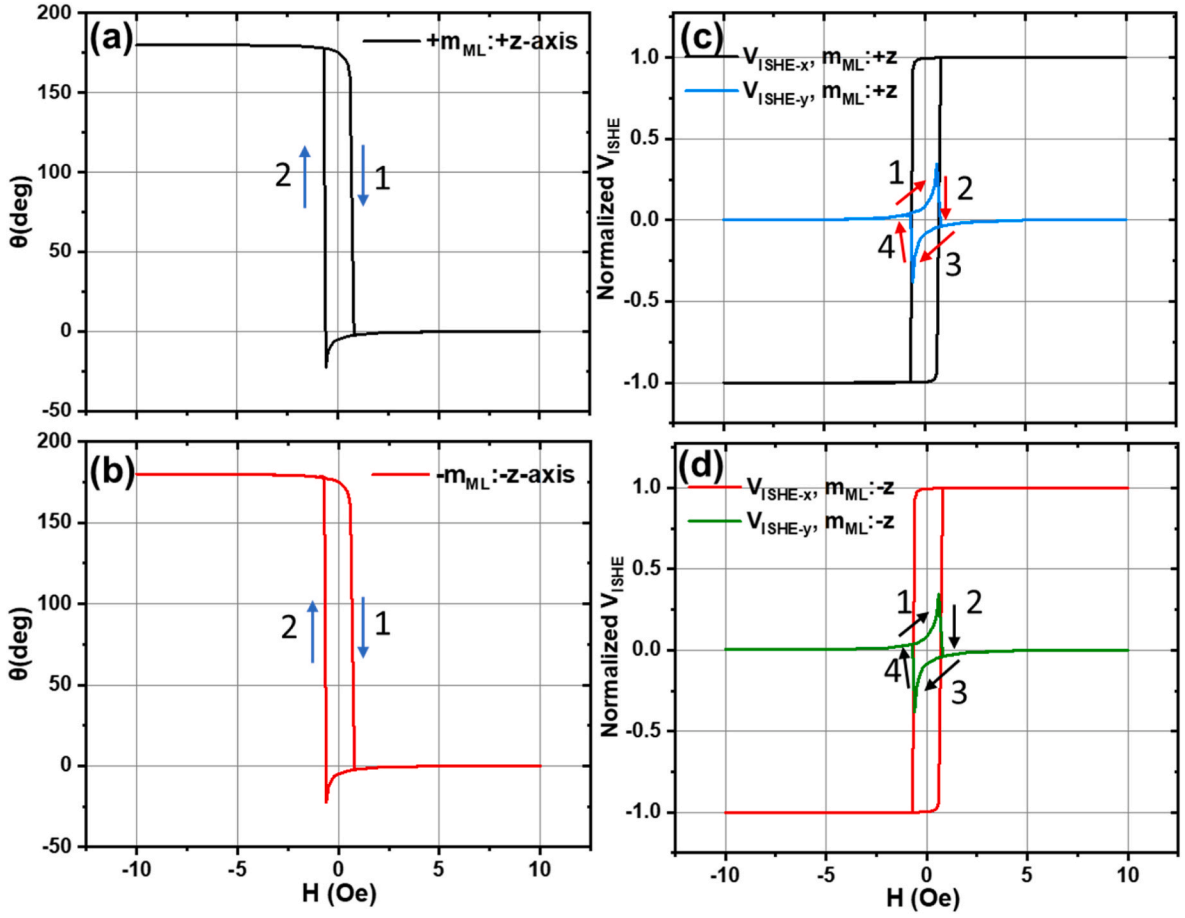

Fig. 5. Theoretical calculated hysteresis loops of θ and V_{ISHE} based on the Stoner-Wohlfarth model when $H_{ML} = 0$. **(a)** and **(b)** are the variations of θ with $\boldsymbol{m}_{\mathrm{ML}}$ initialized along the +z axis and -z axis, respectively. **(c)** and **(d)** display the variations of the normalized $V_{ISHE\text{-}x}$ and $V_{ISHE\text{-}y}$ with $\boldsymbol{m}_{\mathrm{ML}}$ initialized along the +z and -z axes, respectively.

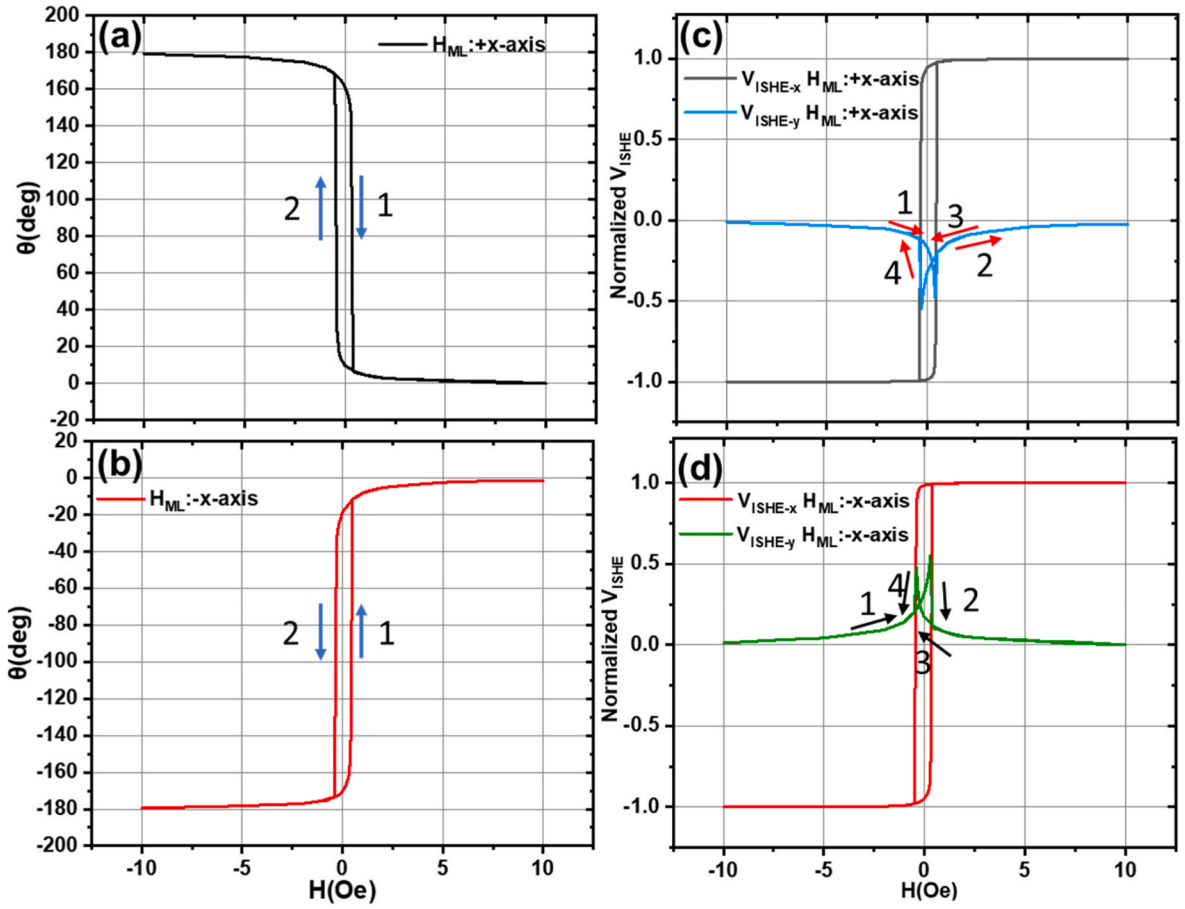

Fig. 6. Theoretical calculated hysteresis loops of θ and V_{ISHE} based on the Stoner-Wohlfarth model when $H_{ML} \neq 0$. **(a)** and **(b)** are the variation of θ with H corresponding to H_{ML} aligned along the positive or negative x-axis. **(c)** and **(d)** are the normalized $V_{ISHE\text{-}x}$ and $V_{ISHE\text{-}y}$ varies with H_{ML} aligned along the positive or negative x-axis.

remain unaffected by the direction of $\boldsymbol{m}_{ML}$.

In contrast, when $H_{ML} \neq 0$, θ follows opposite path as the orientation of H_{ML} changes from the positive x-axis to the negative x-axis, as shown in Fig. 6(a) and (b). The corresponding V_{ISHE} loops are displayed in Fig. 6 (c) and (d). Notably, in this case, $V_{ISHE\text{-}y}$ exhibits butterfly-shaped loops instead of antisymmetric ones, and their directions reverse when the direction of H_{ML} changes. Additionally, the coercivity observed in these loops is smaller than that when $H_{ML} = 0$ (Fig. 5(c) and (d)), which aligns with the experimental results.

Based on the above analysis, the direction of M is influenced by three competing factors, which effectively explain our experimental observations. One factor is the uniaxial anisotropy characterized by K, while the other two stem from H and H_{ML}. When H exceeds approximately 1 Oe, the magnetization of YIG saturates, aligning the M vector with the direction of H. However, when H is below the coercivity of YIG, the direction of M is determined collectively by H, the anisotropy of YIG, and H_{ML}. In the case where $H_{ML} = 0$, the direction of M is governed by H and the anisotropy of YIG.

4. Conclusion

By measuring V_{ISHE} in the YIG/Pt/Co/Pt heterostructure with different device geometries, we experimentally confirmed the presence of a non-zero V_{ISHE} along the direction of the external magnetic field. Our theoretical analysis suggests that this phenomenon is primarily due to the in-plane magnetic anisotropy of single-crystalline YIG. Additionally, we demonstrated that the ISHE voltage loop can be manipulated by modulating the in-plane magnetization component of the Pt/Co/Pt multilayers, which couples with the YIG magnetization. The method used in this study exhibits sensitivity in detecting weak coupling between two ferromagnetic layers with mutually perpendicular magnetization, and it has potential applications in ultra-sensitive magnetic sensors.

CRediT authorship contribution statement

Feiyan Hou: Writing – original draft, Investigation, Formal analysis, Data curation. **Meiling Xu:** Investigation, Data curation. **Xuegang Chen:** Resources. **Yong Dong:** Resources. **Xiufeng Han:** Resources. **Tao Li:** Writing – review & editing, Project administration, Funding acquisition, Formal analysis. **Xiangrong Wang:** Validation, Investigation. **Tai Min:** Project administration, Investigation.

Declaration of competing interest

The authors declare no competing interests.

Data availability

Data will be made available on request.

Acknowledgment

This work was financially supported by the National Key R&D Program of China (Grants No. 2021YFA1202200, 2022YFB4400200), and the Major Key Project of Peng Cheng Laboratory under grant

PCL2023AS1-2.

Appendix A. Supplementary data

Supplementary data to this article can be found online at https://doi.org/10.1016/j.physb.2024.416542.

References

[1] M.I. Dyakonov, V.I. Perel, Current-induced spin orientation of electrons in semiconductors, Phys. Lett. 35 (1971) 459–460.
[2] J.E. Hirsch, Spin Hall effect, Phys. Rev. Lett. 83 (1999) 1834.
[3] J. Sinova, S.O. Valenzuela, J. Wunderlich, C.H. Back, T. Jungwirth, Spin Hall effects, Rev. Mod. Phys. 87 (2015) 1213.
[4] J. Puebla, J. Kim, K. Kondou, Y. Otani, Spintronic devices for energy-efficient data storage and energy harvesting, Commun. Mater. 1 (2020) 24.
[5] A. Azevedo, L. Vilela Leão, R. Rodriguez-Suarez, A.d. Oliveira, S. Rezende, Dc effect in ferromagnetic resonance: evidence of the spin-pumping effect? J. Appl. Phys. 97 (2005) 10C715.
[6] E. Saitoh, M. Ueda, H. Miyajima, G. Tatara, Conversion of spin current into charge current at room temperature: inverse spin-Hall effect, Appl. Phys. Lett. 88 (2006) 182509.
[7] H. Bai, Y.C. Zhang, Y.J. Zhou, P. Chen, C.H. Wan, L. Han, W.X. Zhu, S.X. Liang, Y. C. Su, X.F. Han, F. Pan, C. Song, Efficient spin-to-charge conversion via altermagnetic spin splitting effect in antiferromagnet RuO_2, Phys. Rev. Lett. 130 (2023) 216701.
[8] A. Azevedo, L.H. Vilela-Leão, R.L. Rodríguez-Suárez, A.F. Lacerda Santos, S. M. Rezende, Spin pumping and anisotropic magnetoresistance voltages in magnetic bilayers: theory and experiment, Phys. Rev. B 83 (2011) 144402.
[9] L. Bai, P. Hyde, Y.S. Gui, C.M. Hu, V. Vlaminck, J.E. Pearson, S.D. Bader, A. Hoffmann, Universal method for separating spin pumping from spin rectification voltage of ferromagnetic resonance, Phys. Rev. Lett. 111 (2013) 217602.
[10] L. Liu, T. Moriyama, D.C. Ralph, R.A. Buhrman, Spin-torque ferromagnetic resonance induced by the spin Hall effect, Phys. Rev. Lett. 106 (2011) 036601.
[11] K. Nakahashi, K. Takaishi, T. Suzuki, K. Kanemoto, Power-dependent characteristics of spin current transfer in metal bilayer devices under high-power pulse excitation, ACS Appl. Mater. Interfaces 14 (18) (2022) 21217.
[12] T. Bracher, M. Fabre, T. Meyer, T. Fischer, S. Auffret, O. Boulle, U. Ebels, P. Pirro, G. Gaudin, Detection of short-waved spin waves in individual microscopic spin-wave waveguides using the inverse spin Hall effect, Nano Lett. 17 (2017) 7234–7241.
[13] L. Huang, Y. Zhou, H. Qiu, H. Bai, C. Chen, W. Yu, L. Liao, T. Guo, F. Pan, B. Jin, C. Song, Antiferromagnetic inverse spin Hall effect, Adv. Mater. 34 (2022) 2205988.
[14] M. Kimata, H. Chen, K. Kondou, S. Sugimoto, P.K. Muduli, M. Ikhlas, Y. Omori, T. Tomita, A.H. MacDonald, S. Nakatsuji, Y. Otani, Magnetic and magnetic inverse spin Hall effects in a non-collinear antiferromagnet, Nature 565 (2019) 627–630.
[15] D. Zhang, L. Jin, H. Zhang, Q. Yang, Y. Rao, Q. Wen, T. Zhou, C. Liu, Z. Zhong, J. Q. Xiao, Chemical epitaxial growth of nm-thick yttrium iron garnet films with low Gilbert damping, J. Alloys Compd. 695 (2017) 2301–2305.
[16] X. Liang, Y. Zhu, B. Peng, L. Deng, J. Xie, H. Lu, M. Wu, L. Bi, Influence of interface structure on magnetic proximity effect in Pt/$Y_3Fe_5O_{12}$ heterostructures, ACS applied materials & interfaces 8 (12) (2016) 8175–8183.
[17] M.B. Jungfleisch, V. Lauer, R. Neb, A.V. Chumak, B. Hillebrands, Improvement of the yttrium iron garnet/platinum interface for spin pumping-based applications, Appl. Phys. Lett. 103 (2013) 022411.
[18] M.B. Jungfleisch, A.V. Chumak, V.I. Vasyuchka, A.A. Serga, B. Obry, H. Schultheiss, P.A. Beck, A.D. Karenowska, E. Saitoh, B. Hillebrands, Temporal evolution of inverse spin Hall effect voltage in a magnetic insulator-nonmagnetic metal structure, Appl. Phys. Lett. 99 (2011) 182512.
[19] N. Vlietstra, J. Shan, V. Castel, J. Ben Youssef, G.E.W. Bauer, B.J. van Wees, Exchange magnetic field torques in YIG/Pt bilayers observed by the spin-Hall magnetoresistance, Appl. Phys. Lett. 103 (2013) 032401.
[20] T. Kimura, Y. Otani, T. Sato, S. Takahashi, S. Maekawa, Room-temperature reversible spin Hall effect, Phys. Rev. Lett. 98 (2007) 156601.
[21] C. Du, H. Wang, F. Yang, P.C. Hammel, Enhancement of pure spin currents in spin pumping $Y_3Fe_5O_{12}$/Cu/metal trilayers through spin conductance matching, Phys. Rev. Appl. 1 (2014) 044004.
[22] W.S. Aljuaid, S.R. Allen, A. Davidson, X. Fan, Free-layer-thickness-dependence of the spin galvanic effect with spin rotation symmetry, Appl. Phys. Lett. 113 (2018) 122401.
[23] X.R. Wang, Anomalous spin Hall and inverse spin Hall effects in magnetic systems, Commun. Phys. 4 (1) (2021) 55.
[24] T.C. Chuang, D. Qu, S.Y. Huang, S.F. Lee, Magnetization-dependent spin Hall effect in a perpendicular magnetized film, Phys. Rev. Research 2 (2020) 032053.
[25] J. Holanda, H. Saglam, V. Karakas, Z. Zang, Y. Li, R. Divan, Y. Liu, O. Ozatay, V. Novosad, J.E. Pearson, A. Hoffmann, Magnetic damping modulation in $IrMn_3$/$Ni_{80}Fe_{20}$ via the magnetic spin Hall effect, Phys. Rev. Lett. 124 (8) (2020) 087204.
[26] A. Yagmur, S. Sumi, H. Awano, K. Tanabe, Magnetization-dependent inverse spin Hall effect in compensated ferrimagnet TbCo alloys, Phys. Rev. B 103 (2021) 214408.
[27] M. Yang, B. Miao, J. Cheng, K. He, X. Yang, Y. Zeng, Z. Wang, L. Sun, X. Wang, A. Azevedo, S. Bedanta, H. Ding, Anomalous inverse spin Hall effect in perpendicularly magnetized Co/Pd multilayers, Phys. Rev. B 105 (22) (2022) 224426.
[28] F.J. Chang, J.G. Lin, S.Y. Huang, Robust spin current generated by the spin Seebeck effect, Phys. Rev. Mater. 1 (2017) 031401.
[29] C. Tang, M. Aldosary, Z. Jiang, H. Chang, B. Madon, K. Chan, M. Wu, J.E. Garay, J. Shi, Exquisite growth control and magnetic properties of yttrium iron garnet thin films, Appl. Phys. Lett. 108 (2016) 102403.
[30] N. Nagaosa, J. Sinova, S. Onoda, A.H. MacDonald, N.P. Ong, Anomalous Hall effect, Rev. Mod. Phys. 82 (2010) 1539–1592.
[31] M. Reichling, H. Grönbeck, Harmonic heat flow in isotropic layered systems and its use for thin film thermal conductivity measurements, J. Appl. Phys. 75 (1994) 1914–1922.
[32] K.-i. Uchida, H. Adachi, T. Ota, H. Nakayama, S. Maekawa, E. Saitoh, Observation of longitudinal spin-Seebeck effect in magnetic insulators, Appl. Phys. Lett. 97 (2010) 172505.
[33] M. Weiler, M. Althammer, F.D. Czeschka, H. Huebl, M.S. Wagner, M. Opel, I. M. Imort, G. Reiss, A. Thomas, R. Gross, S.T. Goennenwein, Local charge and spin currents in magnetothermal landscapes, Phys. Rev. Lett. 108 (2012) 106602.
[34] M. Gamino, J.G.S. Santos, A.L.R. Souza, A.S. Melo, R.D. Della Pace, E.F. Silva, A. B. Oliveira, R.L. Rodríguez-Suárez, F. Bohn, M.A. Correa, Longitudinal spin Seebeck effect and anomalous Nernst effect in CoFeB/non-magnetic metal bilayers, J. Magn. Magn Mater. 527 (2021) 167778.
[35] T. Kikkawa, K. Uchida, S. Daimon, Y. Shiomi, H. Adachi, Z. Qiu, D. Hou, X.F. Jin, S. Maekawa, E. Saitoh, Separation of longitudinal spin Seebeck effect from anomalous Nernst effect: determination of origin of transverse thermoelectric voltage in metal/insulator junctions, Phys. Rev. B 88 (2013) 214403.
[36] B.F. Miao, S.Y. Huang, D. Qu, C.L. Chien, Absence of anomalous Nernst effect in spin Seebeck effect of Pt/YIG, AIP Adv. 6 (2016) 015018.
[37] D. Ellsworth, L. Lu, J. Lan, H. Chang, P. Li, Z. Wang, J. Hu, B. Johnson, Y. Bian, J. Xiao, R. Wu, M. Wu, Photo-spin-voltaic effect, Nat. Phys. 12 (2016) 861–866.
[38] G. Li, R.V. Mikhaylovskiy, K.A. Grishunin, J.D. Costa, T. Rasing, A.V. Kimel, Laser induced THz emission from femtosecond photocurrents in Co/ZnO/Pt and Co/Cu/Pt multilayers, J. Phys. D Appl. Phys. 51 (2018) 134001.
[39] H.S. Qiu, K. Kato, K. Hirota, N. Sarukura, M. Yoshimura, M. Nakajima, Layer thickness dependence of the terahertz emission based on spin current in ferromagnetic heterostructures, Opt Express 26 (2018) 15247–15254.
[40] J. Gorchon, S. Mangin, M. Hehn, G. Malinowski, Is terahertz emission a good probe of the spin current attenuation length? Appl. Phys. Lett. 121 (2022) 012402.
[41] T.J. Huisman, R.V. Mikhaylovskiy, J.D. Costa, F. Freimuth, E. Paz, J. Ventura, P. P. Freitas, S. Blugel, Y. Mokrousov, T. Rasing, A.V. Kimel, Femtosecond control of electric currents in metallic ferromagnetic heterostructures, Nat. Nanotechnol. 11 (2016) 455–458.
[42] E.C. Stoner, E. Wohlfarth, A mechanism of magnetic hysteresis in heterogeneous alloys, Philos. Trans. R. Soc. A, Phys. Math. Eng. Sci. 240.826 (1948) 599–642.